A copper silicide nanofoam current collector for directly grown Si nanowire network and their application as lithium-ion anodes

Ibrahim Saana Aminu, HUGH GEANEY, Sumair Imtiaz, Temilade Esther Adegoke, Nilotpal Kapuria, Gearoid A. Collins, KEVIN M. RYAN

Publication date

01-01-2020

Published in

Advanced Functional Materials;30 (38)

WILEY-VCH

DOI: 10.1002/((please add manuscript number))

Article type: Full Paper

Title: A Copper Silicide Nanofoam Current Collector for Directly Grown Si Nanowire Networks and their Application as Lithium-ion Anodes

*Ibrahim Saana Aminu, Hugh Geaney, Sumair Imtiaz, Temilade E. Adegoke, Nilotpal Kapuria, Gearoid A. Collins, Kevin M. Ryan**

Dr. I. S. Aminu, Dr. H. Geaney, S. Imtiaz, T. E. Adegoke, N. Kapuria, G. A Collins, Prof. K. M. Ryan

Bernal Institute, University of Limerick, Limerick V94 T9PX, Ireland

Department of Chemical Sciences, University of Limerick, Limerick V94 T9PX, Ireland

E-mail: kevin.m.ryan@ul.ie, Phone: +353-61 213167

Keywords: 3D Cu_xSi_y nanofoam, silicon nanowires, high density, areal capacity, lithium-ion battery

Abstract: Silicon nanowires (Si NWs) have been identified as an excellent candidate material for replacement of graphite in anodes, allowing for a significant boost in the capacity of LIBs. Herein, high-density Si NWs are grown on a novel 3D interconnected network of binary-phase Cu-silicide nanofoam (3D Cu_xSi_y NF) substrate. The nanofoam facilitates uniform distribution of well-segregated and small-sized catalyst seeds, leading to high-density/single-phase Si NW growth with an areal-loading in excess of 1.0 mg cm^{-2} and a stable areal capacity of ~2.0 mAh cm^{-2} after 550 cycles. The use of the 3D Cu_xSi_y NF as a substrate is further extended for Al, Bi, Cu, In, Mn, Ni, Sb, Sn and Zn mediated Si NW growth, demonstrating the general applicability of the anode architecture.

1. Introduction

Silicon (Si) is on the verge to become a realistic substitute to graphite in lithium-ion batteries (LIBs). However, notwithstanding its high theoretical capacity (3,579 mAh g^{-1}),[1-4] the full-scale implementation of Si only anodes in LIBs is yet to be realised. The unrestrainable volume expansion of Si (>300%) upon cycling can lead to pulverization, delamination-induced loss of contact with the current collector (CC), and an unrecoverable capacity loss in bulk, films, and micron-sized particles based anodes.[4, 5] The use of sub-micron sized pillars and nanocomposite architectures have only yielded limited improvements.[4, 6] Despite that various attempts have been made toward resolving these issues, mechanical instability of the active materials/CC interface, low yields, and long-term continuous capacity-fade remain a challenge.[2, 4, 7] Fortunately, one-dimensional silicon (nanowires) can circumvent these issues because of the ability to accommodate large strains without shattering. Nanowires and their interconnected networks (formed after cycling) also possess a relatively high surface area,[2, 8] provide shorter ion diffusion distance, improved electronic transport, afford large

electrode/electrolyte contact area for reduced charge time, and can be directly grown on CCs.[2-4, 8]

Direct growth of Si nanowires (Si NWs) on CCs is particularly attractive for high battery performance at reduced cost (*e.g.* for electric vehicles) due to the ability to exclude inactive polymeric binders/conductive additives, reduce weight, and enhance stability of NWs/CC contact.[2, 4, 9, 10] Copper (Cu) is 40 times more conductive than stainless steel (SS) with a stable potential window, and is widely accepted as a suitable CC for LIBs. However, its application for direct growth of Si NWs is hampered by the energetically favourable formation of large crystallite grains and/or nanowire based Cu-Si compounds,[11, 12] that are inactive for Li-cycling.[13, 14] The formation of micron-sized crystallite grains limits the ability to directly grow robust and pure phase Si NWs on Cu substrates. Traditional electrodes prepared with polymeric binders, conductive additives and Si on Cu-substrates are also prone to Si expansion-induced stresses, which can lead to interface fragmentation and loss of electric contact. Therefore, stainless steel (SS), metal (Ni)-foams and porous carbons have been adopted as alternatives CCs to grow Si NWs.[2, 4, 8, 9, 15-18] However, even as these CCs offer various advantages, they present a number of challenges. For example, the low surface area of planar metal foils is not ideal for achieving the much needed high Si NW loading,[9, 19] and often results in low yields (*e.g.* 0.18 – 0.4 mg cm^{-2}).[1, 2, 4, 9, 18, 20] The electrical and mechanical properties of carbon based-substrates are also inferior. Thus, achieving high areal-loading with adequate mechanical/electrical properties on these common substrates still remains difficult. An attempted growth of Si NWs on bulk Cu by chemical vapour deposition at 650 ^{o}C resulted in NWs that easily delaminate from the substrate, leading to poor anode performance.[17] Conversely, metal (*e.g.* Ni, Cu) foams can facilitate high NW growth owing to their relatively high surface area compared to planar and bulk counterparts.[16, 17] However, in addition to their

undesirably high thickness, they are much heavier than a standard battery Cu-foil and also easily lose their mechanical strength, making them practically unsuitable for use in batteries. Alternative anode architectures based on mixing Si nanoparticles with Si NWs, Si-thin films, Mxene, graphene, and CNTs or core/shell Si NWs@C networks with porous nanostructures, have also been explored[1, 20-27]. However, most of these anodes still rely on either traditional slurry or conventional multi-layer deposition procedures.

The direct growth of single phase, alloyed and heterostructured Si NWs has been widely explored using gold as a catalyst.[3, 4, 10, 18, 28, 29] However, the adverse impact of gold on the electrical properties of Si, in addition to its low NW yields, high cost, weight, and inactive participation in Li-cycling,[7, 30] have rendered it unattractive. In contrast, tin (Sn) is relatively cheaper and not only effective for catalysing Si NW growth, but can also actively participate in the Li-cycling activity (theoretical capacity, Sn: 994 mAh g^{-1}).[1, 31] Simultaneously achieving high-density (high areal-loading and good CC surface coverage) of directly grown Si NWs on a mechanically robust and highly conductive Cu-based CC is desirable to show the viability of directly grown Si NWs for real world application.[2, 32]

Herein, for the first time, we show that an intermediate single layer of interconnected Cu-silicide (Cu_xSi_y) network, grown *in situ* on a planar Cu-foil, can facilitate high-density Si NW growth (**Figure 1**) with higher areal-loadings than common CCs. The obtained network structure offers significant advantages over metal foam and planar metal (Cu, SS, Ni)-foil CCs, including: (*i*) intrinsic nanowire features that facilitate high-density deposition of small-sized, well-segregated and uniform distribution of catalyst seeds, (*ii*) inherent electrical properties, as an intermetallic, to benefit electronic transport and charge distribution, (*iii*) an interconnected network structure which provides excellent surface and mechanically robust anchor sites for high-density Si NW attachment and stability, and (*iv*) a lateral network structure to circumvent

the formation of any grain-sized Cu/Si compounds during Si NW growth by restricting concomitant atomic Cu diffusion, thus, making it possible to grow high-density, pure phase, and robust Si NWs.

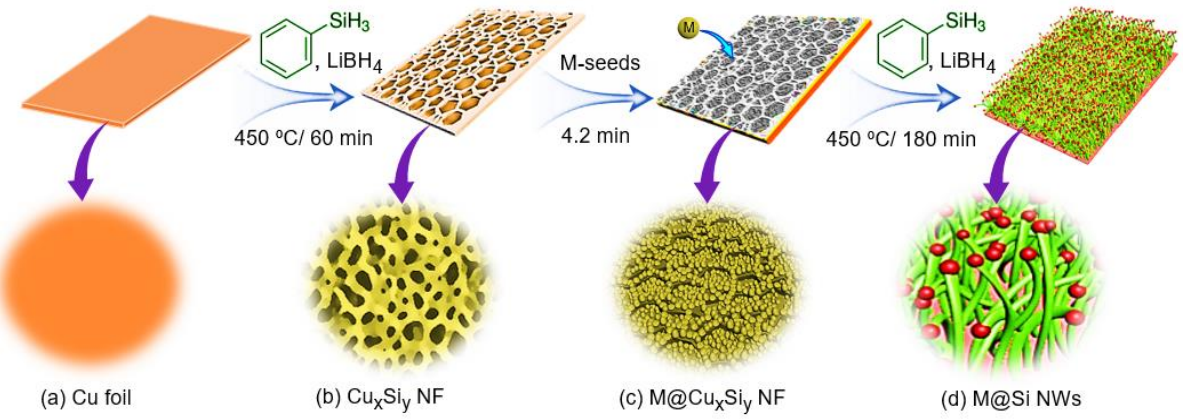

Figure 1 Schematic illustration of the synthesis of the 3D Cu_xSi_y NF and high-density M-seeded Si NWs, a) plain Cu-foil, b) formation of binary-phase 3D Cu_xSi_y NF, c) M-seeds decorated 3D Cu_xSi_y NF, and d) high-density M-seeded-Si NWs growth on the 3D Cu_xSi_y NF. (M = Al, Bi, Cu, In, Mn, Ni, Sb, or Zn). All reaction steps were carried out in a glove box under Ar atmosphere.

2. Morphology, Structure and Composition

Figure 2a and **Figure S1** (Supporting Information) show the *ex situ* SEM images of the 3D Cu_xSi_y NF, revealing a monolayer of well-defined and interconnected network morphology with average sizes of ~140 nm (branches) and ~420 nm (voids). It is worth noting that this feature size is significantly smaller by over ~450 fold compared to a typical Cu or Ni foam (**Figure S2**, Supporting Information), and is more suitable for high-density Si NW support. Cross-sectional analysis by focused ion beam (FIB)-SEM (**Figure S3**, Supporting Information) further reveal that the Cu_xSi_y network is interfaced with the parent Cu-foil by an intermediary

Cu-silicide layer. To examine the structure in more detail, an electron-transparent lamella was prepared by FIB milling for TEM analysis. As shown in **Figure 2b**, the Cu_xSi_y network exhibits a crystalline structure with an observable fusion zone between particles at an average angle of ~130°. The atomic arrangements and lattice spacing are clearly revealed by high resolution TEM as shown in **Figure 2c**. The corresponding fast Fourier transform diffractogram (**Figure 2d**) and line profile of atomic ordering (**Figure 2e**) further confirm the high crystallinity of the Cu_xSi_y network. As shown in **Figure S4** (Supporting Information), the interfacial silicide layer also exhibits a crystalline structure similar to that of the Cu_xSi_y network, suggesting the same phase of Cu-silicide, which maybe accountable for the robustness of the 3D Cu_xSi_y NF network.

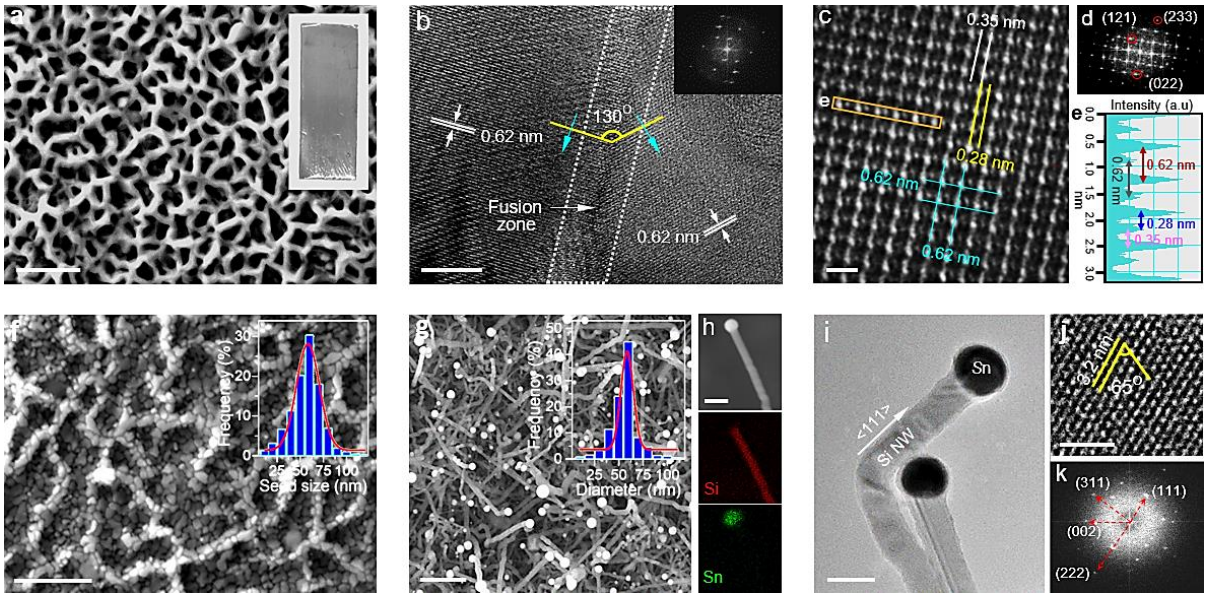

Figure 2 a) SEM image of the 3D Cu_xSi_y NF (scale: 2 µm) and optical photograph of the as prepared sample (inset, size: 3.0 ×1.0 cm, thickness: ~70 µm), b) TEM image of the 3D Cu_xSi_y NF, revealing the fusion between particles (scale: 5 nm) and fast Fourier transform (FFT) diffraction pattern (inset), c) HR-TEM image (scale: 1 nm) and corresponding d) FFT pattern and e) line profile of atomic ordering, f) SEM image of the Sn-seeds decorated 3D Cu_xSi_y NF

(scale: 1 µm), g) SEM image of high-density Sn-seeded Si NWs (scale: 1 µm), h) Elemental mapping of Si and Sn (scale: 100 nm). An inset in Figure (f) and (g) is the Gaussian-fitted histogram of size distribution for the Sn-catalyst seeds and Si NWs, respectively, i) TEM image of Sn-seeded Si NWs (scale: 50 nm) and corresponding j) high resolution TEM image (scale: 2 nm) and k) FFT diffraction pattern.

The as prepared 3D Cu_xSi_y NF was used as a substrate to grow Si NWs. To this end, a thin-layer of tin (Sn) catalyst seeds was coated on the 3D Cu_xSi_y network by thermal evaporation. The obtained Sn-seeds@3D Cu_xSi_y NF assembly (**Figure 2f**) show well-formed and segregated small-sized Sn-seeds uniformly decorated on both the network branches and mesh-spaces. The average seed-size is ~60 nm, which is also slightly smaller compared to a ~72 nm size when deposited on commercial Cu-foam (**Figure S5**, Supporting Information). Such a uniform distribution of nanosized Sn catalyst seeds on the 3D Cu_xSi_y NF can enable high-density Si NW growth compared to the largely fused and uneven seed dispersion when deposited on planar Cu foil (**Figure S6**, Supporting Information). Besides the Sn seeds, Al (~22 nm), Zn (~34 nm) and In (~40 nm) deposition also yielded smaller, high-density, and uniform nanosized seed distribution on the 3D Cu_xSi_y NF (**Figure S7**, Supporting Information), further indicating its suitability toward a wide range of catalysts for a variety of high density Si NW synthesis. The SEM image of Sn-catalysed Si NWs on the 3D Cu_xSi_y NF (**Figure 2g**) and the low magnification in **Figure S8 (**Supporting Information) clearly display high-density of NWs with an excellent surface coverage. Mapping of elemental distribution (**Figure 2h**) and EDX analysis (**Figure S9**, Supporting Information) confirm the presence of only Si in the NW body without any interatomic alloying with Cu or Sn. This shows the efficiency of the 3D Cu_xSi_y NF to allow for growth of pure phase Si NWs without any metal atom infusion.

Figure 2i shows the TEM image of Si NWs with an average diameter of ~38.9 nm grown in the ⟨111⟩ direction. High resolution of selected areas along the wire reveals lattice arrangements typical of a crystalline Si,[4, 28, 33] exhibiting a lattice spacing of ~0.32 nm and an angle of ~65° between the (111) and (220) planes. X-ray diffraction patterns were also analysed to verify any influence of the Sn-seed and/or the intermediary Cu-silicide structures on the Si NW structure. As shown in **Figure S10** (Supporting Information) the diffraction peak angles seamlessly match that of a pure phase crystalline Si and consistent with previous reports.[1, 4] This further shows that the intermediary silicides significantly inhibited atomic Cu precipitation or diffusion into the Si NW phase, thereby, effectively avoiding any eventual formation of grain-sized Cu/Si compounds while enhancing pure Si NW growth. Besides the intense peaks of the parent Cu, the diffraction patterns also show minor peaks intrinsic to the low temperature equilibrium silicide phases ($Cu_{15}Si_4$ and $Cu_{0.83}Si_{0.17}$), which can be assigned to the Cu_xSi_y network/intermediate layer.[11, 14]

The impact of the 3D Cu_xSi_y NF was carefully verified in a series of control experiments. In this regard, bare Cu-foil, Sn seed-coated planar Cu-foil and the Sn seed-coated commercial Cu-foam were subjected to similar Si NW growth reactions. As shown in **Figure S11** (Supporting Information), the Sn-coated Cu-foil leads to segregated formation of both Si NWs in dotted areas and patchy micron-sized Cu/Si compounds (largely grains), whereas the bare Cu-foil yields only large grains of Cu/Si compounds. While metal foams have been used in other methods to grow Si or composite nanowires,[2, 16, 17] our synthesis protocol shows that the Si NWs exhibit a wide range (23–140 nm) of size distribution (**Figure S12**, Supporting Information) in addition to the formation of micron-sized Cu/Si grains in large areas. Most notably, the Cu-foam becomes very fragile and significantly lost its flexibility and mechanical

toughness to robustly support the Si NWs (inset of Figure S12), thus, rendering it as an unsuitable binder-free anode for use in LIBs.

3. Growth Mechanism of the 3D Cu_xSi_y NF Network

Figure 3a shows the schematic for the lateral growth process of the monolayer Cu_xSi_y network, based on experimental observations. The 3D Cu_xSi_y network formation is governed by a spontaneous interatomic diffusion reaction of solid state Cu atoms with flux of vapour phase Si atoms upon phenylsilane (PS) decomposition. Atomic saturation by Cu-Si interdiffusion triggers the formation of a binary-phase Cu-silicide at the Si flux/Cu-foil interface, leading to rapid growth of a thin-layer of Cu-rich silicide, ~180 nm thick within ~30 seconds, as shown in **Figure S13** and **S14** (Supporting Information). After ~5 min of reaction, the precipitation of sphere-like silicide nanoparticles at the Si flux/silicide-layer interface, averaging ~300 nm in size, is observed (**Figure 3b**). The nanoparticle formation is spontaneous with the high possibility of occurrence at defects site and/or grain boundaries as a result of random nucleation processes, leading to a sparse distribution.[34] Continued reaction with flux of Si up to ~10 min leads to manifestation of more silicide nanoparticles via diffusion of Cu from the intermediary silicide layer and/or larger silicide nanoparticles, as suggested by reduction of the average particle size from ~300 to ~85 nm (**Figure 3c**). This phenomenon drives the formation of network channels through a self-aligned interparticle fusion along areas of high particle concentration. Proliferation of the network branches is invigorated by continuous formation of smaller silicide nanoparticles (average size: ~60 nm) up till ~40 min on the growing branches and interbranch spaces (**Figure 3d**). These small silicide nanoparticles are then subsequently adsorbed via a mechanism akin to an Ostwald ripening process.[34] Thus, the emerging network branches (average size: ~114 nm) are more

energetically favoured for fusion-induced incorporation of the small nanoparticles, resulting in the manifestation of a fully-grown monolayer network with an average branch size of ~140 nm (**Figure 3e**).

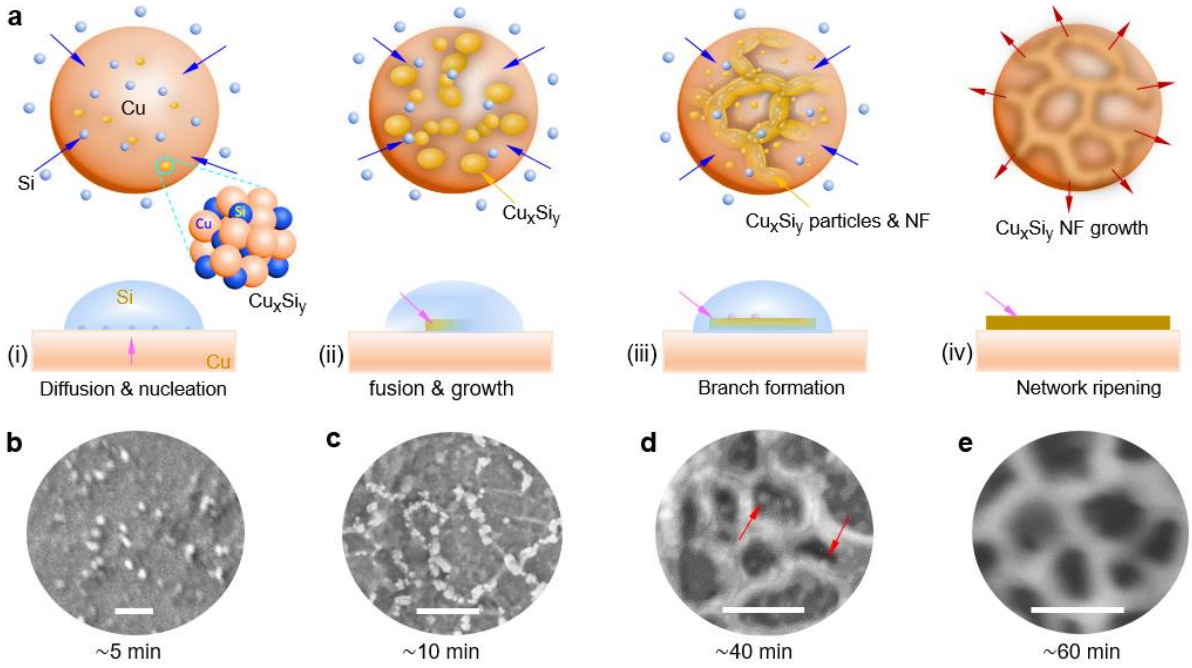

Figure 3 a) Schematic illustration of the formation mechanism and structural transformation steps to the 3D Cu_xSi_y NF and corresponding *ex situ* SEM images (scale: 500 nm) showing the formation of b) spherical nanoparticles, ~300 nm, c) fusion of the nanoparticles into branches, ~85 nm, d) network growth, ~114 nm, red arrows show the fusing of nanoparticles, ~60 nm, on the branches, and e) network ripening, ~140 nm in size. (see more detailed representation in Figure S13).

The strongly adhered Cu_xSi_y network on the Cu-foil surface constitutes the combined feature of a binary-phase 3D nanofoam system (3D Cu_xSi_y NF) and exhibits a uniform distribution of both Si and Cu as shown in **Figure S15** (Supporting Information). The observable time-lapsed

evolution of the 3D Cu_xSi_y network is further demonstrated in **Figure S16** (Supporting Information). It is worth noting that the as grown Cu_xSi_y network is very robust and endured a scotch tape peel-off tests for several times and more than 200 cycles of intense mechanical bending and twisting forces without delamination or any damages (**Figure S17** and **Video S1**, Supporting Information). The robust mechanical properties benefit synergistically from the underlying Cu-foil support and the small-sized interconnected features of the laterally-aligned network branches which could enhance efficient stress distribution and fracture resistance. Such robust properties of the 3D Cu_xSi_y NF can simultaneously address the poor mechanical features of metallic Cu and Ni foam CCs, the low yields/formation of undesirable micron-sized Cu-Si crystallite grains on planar Cu-foils, and the inferior electrical properties of carbon-based substrates. More importantly, the 3D Cu_xSi_y network growth is scalable toward practical application as shown in **Figure S18** (Supporting Information).

4. Optimising the Si NW Density and Areal-Loading

Figure 4a shows the areal-loading of as grown Si NWs on the 3D Cu_xSi_y NF at various PS concentrations (Si flux). The formation of a highly dense Si NWs is observed at ~1.25 mL of PS reaction (inset SEM image) corresponding to an areal-loading of ~1.26 mg cm^{-2}. A critical growth density is seemingly reached beyond which additional PS does not result in further nanowire growth and the areal-loading remains invariant. However, such redundant Si flux leads to the formation of an amorphous layer (**Figure S19**, Supporting Information). On the basis of these observations, it can be deduced that ~(0.8–1.25 mL) of PS is adequate to achieve a sufficiently high-density of Si NWs with areal-loading in excess of 1.0 mg cm^{-2} on the 3D Cu_xSi_y NF based on a ~25 nm thick layer of catalyst seeds within ~150–180 min of reaction. As shown in **Figure 4b**, the areal-loading on the 3D Cu_xSi_y NF is significantly higher

compared to the overall loading on planar Cu-foil and commercial Cu-foam (*i.e.* the Si NWs and crystallite Cu/Si grains combined) as well as stainless steel. Importantly, such high-density growth of Si NWs on the 3D Cu_xSi_y NF is scalable on a large sample as demonstrated in **Figure S20** (Supporting Information), which is desirable for practical application.

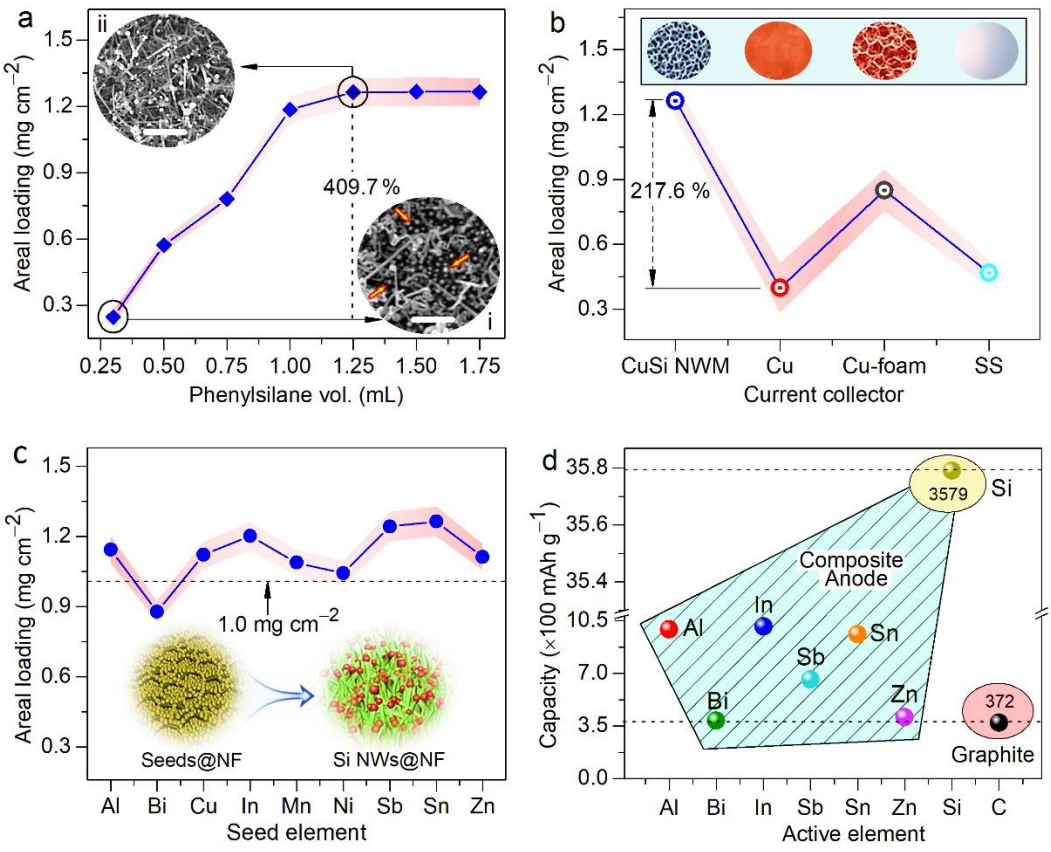

Figure 4 a) Normalised areal-loading of Si NWs grown on the 3D Cu_xSi_y NF at various phenylsilane concentration. An inset is the SEM images of Si NWs (scale: 1 µm) grown with (i) ~0.35 mL and (ii) ~1.25 mL of phenylsilane. Yellow arrows in (i) show underutilised Sn seeds, b) Normalised areal-loading of Si NWs on the 3D Cu_xSi_y NF compared to commonly used metallic CCs. An inset is the corresponding representative image, c) Normalised areal-loading of Si NWs on the 3D Cu_xSi_y NF using various metal seed catalysts. The pinkish shaded regions

of figures a–c is the error bar areal fill and solid lines are a guide to the eye, d) Gravimetric capacity of the seed elements and Si in comparison with graphite as a reference.

Given the significant role of the 3D Cu_xSi_y NF in facilitating efficient Sn-seeded Si NW growth, we further explored its suitability as a universal platform for Si NW growth using various metal seeds. In this regard, all the three classes of known M-catalysts, including the high Si solubility/non-silicide forming catalyst (Al), the low Si solubility/non-silicide forming catalysts (Bi, In, Sb, Zn) and silicide forming catalysts (Cu, Mn Ni) were probed. **Figures S21–28** (Supporting Information) show the successful growth of Si NWs by these metal catalysts under similar synthesis conditions, demonstrating high flexibility and efficiency of the 3D Cu_xSi_y NF for synthesising a variety of Si NWs. As shown in **Figure 4c**, all catalysts (but Bi, due to it low surface tension) facilitate Si NW growth with an areal-loading in excess of 1.0 mg cm^{-2}. Nonetheless, the overall areal-loading of Bi-seeded Si NWs (~0.87 mg cm^{-2}) on the Cu_xSi_y NF is still considerably higher than reported for planar SS (0.18 – 0.32 mg cm^{-2}).[1, 4, 9, 17] The Si NWs also display clearly contrasted seeds at their tips with sizes larger than the wire diameter, except for the Al, Cu, and Mn seeded Si NWs which seemingly exhibit comparable size for both the seeds and wires. Average size (D_{av}) analysis of the Si NWs also suggests a dependence on the seed element. Typically, Bi, Mn and Sb seeded Si NWs exhibit a similar nanowire size of ~50 nm, while Zn and In produced the smallest (D_{av}~17 nm) and largest (D_{av}~70 nm) average nanowire size, respectively (**Figure S29**, Supporting Information). As shown in **Figure 4d**, it is worth nothing that in addition to effectively catalysing Si NW growth Al, Bi, In, Sb, and Zn are lithium active with higher theoretical capacity than graphite[35]

and therefore can contribute to improve anode efficiency and boost battery performance when combined with Si NWs.

5. Li-Cycling Performance

To demonstrate the significance of the 3D Cu_xSi_y NF as an electrode architecture, the Li-cycling capability of M-seeded Si NWs anodes were evaluated. Cyclic voltammetry (CV) profiles of the Sn-seeded Si NWs (**Figure 5a**) and that of selected samples (**Figure S30**, Supporting Information) show similar lithiation/delithiation trends typical of Si NWs and consistent with previous reports.[4, 9, 17, 36] The anodic current and area under the curves increase continuously in successive scans, indicating the activation of more Si NWs to react with Li^+ ions in each succeeding scan with enhanced electrolyte penetration.[2, 4, 36, 37] However, the CV curves tend to overlap beyond 10 cycles (**Figure S31**, Supporting Information), signifying the stabilisation of the Li-cycling mechanism and high reversibility of the lithiation/delithiation processes. The cathodic current peaks at ~0.15V and below 0.1V represent successive lithiated conversion of amorphous and crystalline Si, respectively, resulting in a mixture of *c*-Li_xSi and *a*-Li_xSi at the lower potential limit.[36, 38] The corresponding anodic peaks, reproduced in all the scans at ~0.36 and ~0.55V, also suggest a similar storage mechanism and high reversibility of the anode. The anode also exhibits high charge/discharge performance (**Figure 5b**), attaining a normalized initial gravimetric charge and discharge capacity of ~3,649 and ~2,184 mAh g^{-1}, respectively, which is considerably higher than reported for most Si based anodes (see **Table S1** and **S2**, Supporting information).

As an important consideration for the cycling life and application of LIBs, the behaviour and stability of the Si NWs on the 3D Cu_xSi_y NF post Li-cycling were also examined. The *ex situ* SEM image (**Figure S32**, Supporting Information) shows almost no change in the

Si NW morphology after 10 cycles. However, after 50 cycles the initially smooth nanowire surface becomes textured with an increase in the Si NW size by 145–317% in good agreement with previous reports.[2, 3, 4, 39] Notwithstanding, the Si NWs remain continuous without complete fragmentation as typically observed for Si-nanoparticles, Ge NWs, or Si/Ge heterostructures.[40-43] More importantly, the NWs remain in good contact with the 3D Cu_xSi_y NF substrate without delamination (**Figure S33**, Supporting Information). This is essential for facilitating continuous electron transport during cycling while minimising capacity fade due to electrical-disconnect, thereby, maintaining a stable performance. The impact of the anode composition and architecture on the capacity was also evaluated. As shown in **Figure 5c**, both Cu-foam and Cu-foil based anodes exhibit a significantly lower capacity than the theoretical value (Si ~3,579 mAh g^{-1}) compared to the 3D Cu_xSi_y NF based anode which benefits from the robust interconnected architecture (Si NWs@Cu_xSi_y@Cu) and excellent contact with the highly conductive Cu-foil.

The anode also exhibits a stable rate capability performance at varying C-rates from 0.1C to 10C (**Figure 5d**). It is evident that the anode upholds the rate performance with only a slight depletion at faster rates, retaining a reversible capacity greater than ~1100 and ~750 mAh g^{-1} at 5C and 10C, respectively. It is worth noting that the capacity not only fully recovers when the rate bounces abruptly from the high rate of 10C to the initial 0.1C, but also maintains a steady cycling performance beyond 300 cycles with the Cuolombic efficiency (CE) increasing from ~66.0% to above ~99.0%, indicating the stabilisation of the solid electrolyte interface (SEI) and high reversibility of the anode. The initial CE can potentially be further enhanced through pre-lithiation, nanocarbon sheathing or use of artificial-SEI layers.[1, 3, 22] This rate performance is indicative of the robustness of the anode architecture which effectively enhances the kinetics of the lithiation/delithiation process. As shown in **Figure 5e**,

the enhanced features also confer the anode with a very stable charged capacity extending beyond 500 cycles, leading to a high areal capacity of ~2 mAh cm^{-2} after 550 cycles (inset figure) and a high retentive discharge capacity of ~75.8%. The combined synthesis protocol and electrochemical properties of this anode compare favourably with reported binder-free Si and even composite-Si NW anodes, including conventional slurry based anodes that used binders and conductive additives as displayed in **Table S1** and **S2** (Supporting information), thus, highlighting the high promise of the 3D Cu_xSi_y NF for LIBs application.

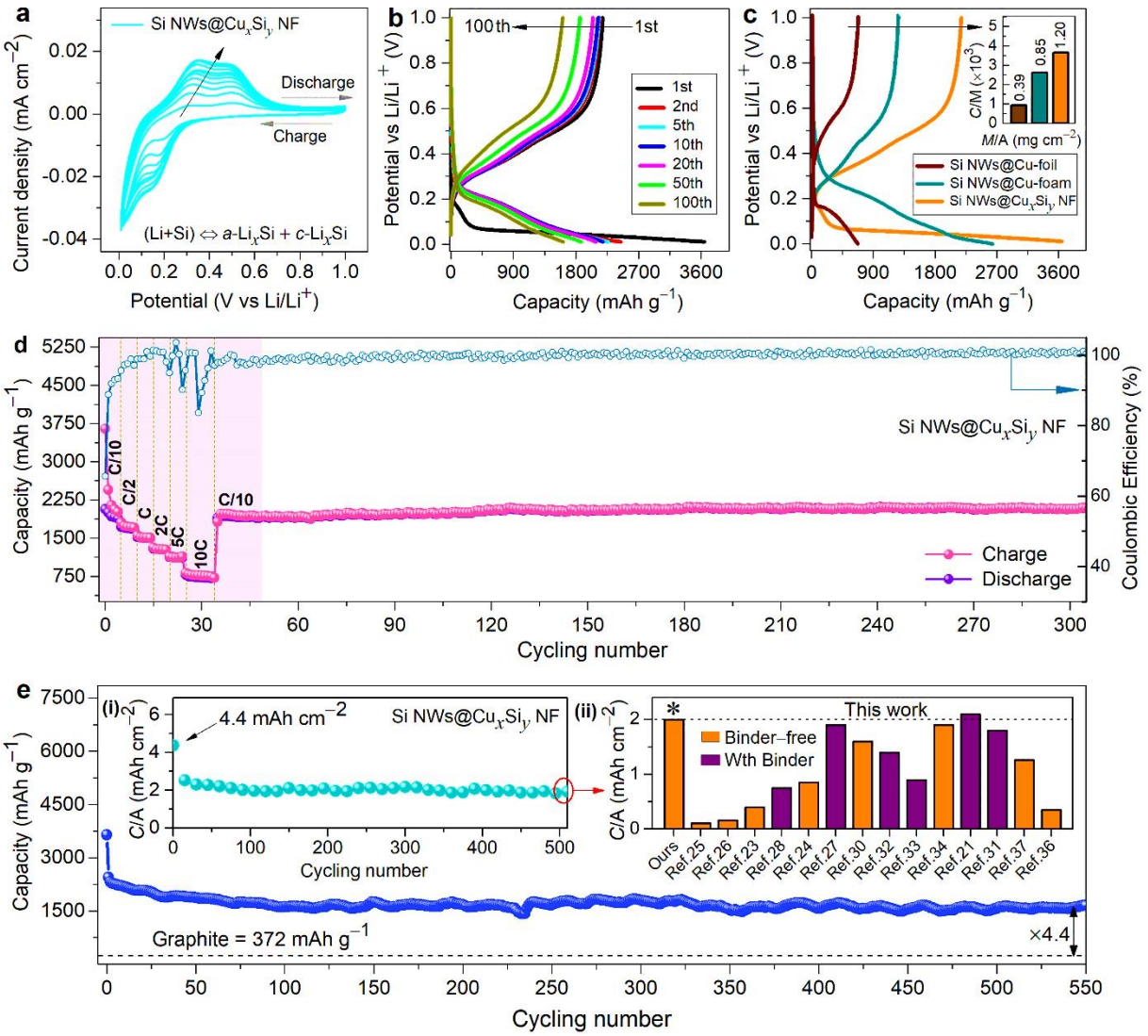

Figure 5 Electrochemical performance of the Sn-seeded Si NWs@Cu_xSi_y NF. a) Cyclic voltammetry profiles, b) Galvanostatic charge/discharge capacity profile, c) Galvanostatic charge/discharge capacity profiles of various anodes, an inset figure indicates the charge capacity and average areal-loading (number on bars), d) Rate capability at various C-rates, e) long-life cycling stability. An inset figure is (i) areal capacity (at every 15th cycle) and (ii) A comparison of post-cycling areal capacity of various Si-anodes, details of the references are stated in the supporting information.

6. Conclusion

In summary, a highly flexible and mechanically robust binary-phase 3D Cu_xSi_y nanofoam is developed as a universal binder-free CC for efficient growth of high-density Si NWs with high areal-loading. While in most systems the intermediate formation of copper silicide particles is undesirable, we have successfully controlled the silicide formation to leverage its optimal properties by constraining it to occur in a 2D network structure. The nanofoam network exhibits excellent mechanical robustness and facilitates not only a control of the catalyst seed size and distribution, but also enabled high areal-loading and stable Si NW growth for all the three classes of catalyst. The combined properties of the 3D Cu_xSi_y NF leads to a stable Si NW anode with a gravimetric and areal capacities that are significantly higher than several reported Si NW based anodes. This work, thus, offers an attractive and versatile approach for development of robust alloying nanowire anode architecture for lithium ion batteries.

7. Experimental Section

Synthesis of 3D Cu_xSi_y NF: Typically, a copper foil (~99.9% metal basis) was surface graded using P600 grit sandpaper and ultrasonically washed in methylbenzene (MePh) to remove surface impurities, oxide layers and to increase the surface area for maximum reactivity. A strip of the treated foil (1.0 × 3.0 cm) was then diagonally placed in a 20 mL capacity cylindrical glass vial containing 0.5 mL of squalane (SQL: ~96%). The solution was then placed on a hotplate (Stuart® CD-162) and ramped to 450 °C and kept to boil for 15 min, followed by injecting 0.05 mL of phenylsilane (PS: ~97%) and then allowed to react for 5 min. 2–3 microneedle-drops of a reducing agent ($LiBH_4$: 2M in tetrahydrofuran) was injected to enhance the PS decomposition. The reaction was then allowed to proceed for ~55 min before being quenched by switching off the hotplate and directly removing the substrate. The pinkish-orange Cu-foil turned to light-gray in colour, indicating formation of the copper-silicide nanofoam (Cu_xSi_y NF, average mass: ~0.2 mg). The product was then thoroughly rinsed in MePh, dried and stored under Ar-atm. in the glovebox (< 0.1 ppm O_2 /H_2O) until further used. The reaction time was carefully varied at certain time intervals (0.5 – 60 min) to monitor the evolution mechanism of the Cu_xSi_y NF morphology.

Preparation of catalyst seed decorated 3D Cu_xSi_y NF: Typically, a ~25 nm thick layer of tin (Sn, ~99.999%, Kurt J. Lesker) catalyst seeds was thermally evaporated on to the surface of the as-synthesised Cu_xSi_y NF. For this deposition, an Ar-filled glovebox-based thermal evaporator system (Mbrun, MB-200B) operated at ~5.0×10^{-6} bar of vacuum pressure was used. To avoid atmospheric oxidation, the Sn-seed coated Cu_xSi_y NF was stored in the Ar-filled glovebox (< 0.1 ppm O_2 /H_2O) until further used. A similar procedure was applied for deposition of various metal seeds, including Al, Bi, Cu, In, Mn, Ni, Sb and Zn catalyst.

Synthesis of Si nanowires: High-density Sn-seeded Si NWs (Sn@Si NWs) were synthesised based on the vapour-liquid-solid (VLS) epitaxial growth mechanism in the solution phase, using the as-prepared Sn-coated 3D Cu_xSi_y NF as the growth substrate. Typically, four samples (0.7 × 0.7 cm) were placed horizontally/face-up in a closed cylindrical glass vial (35 mL capacity) containing ~1.5 mL dry squalane solution and then placed on the above hotplate. The temperature was ramped to 450 ^oC and kept boiling for 15 min, followed by sequential injection of PS (0.25 – 0.5 mL) and $LiBH_4$ (3 microneedle drops). The reaction was allowed to proceed undisturbed for ~55 min followed by another injection of PS (0 – 1.25 mL) for another ~110 min before turning off the hotplate and allowed to cool naturally to room temperature prior to substrate removal. The product was rinsed in MePh and dried under vacuum before characterisation. As a control experiment, Sn-seeds were directly deposited on planar Cu-foil and commercial Cu-foam and then subjected to similar treatment for Si NW growth. A further experiment with a bare planar Cu substrate was performed for comparison. The areal-loading of the obtained Sn-seeded-Si NWs on the Cu_xSi_y NF reached ~1.26 mg cm^{-2} with complete surface coverage. The mass of samples was determined using a microbalance (Sartorius SE2, ±0.25μg repeatability) for measuring the mass of bare Cu-foil, 3D Cu_xSi_y NF, catalyst seed-coated 3D Cu_xSi_y NF and then after Si NW growth. All reactions steps including washing and drying were carried out in an Ar-filled glovebox (< 0.1 ppm O_2 /H_2O).

Characterisation and measurements: Field emission scanning electron microscopy (SEM) analysis was carried out using SU70 Hitachi (MSB-011) fitted with an energy dispersive spectrum (EDX) analyser (Oxford instruments) and operated at 5–20 kV. All sample were directly analysed without further treatment. Cross-sectional analysis was performed using a focused ion beam (FIB) milling technique carried out on a FEI Helios G4 CX microscope

equipped with an EDX analyser and operated at 5–10 kV. Transmission electron microscopy (TEM) analysis was performed on JEOL JEM-2100F (MSB-005) equipped with a Gatan Ultrascan CCD camera and an EDAX Genesis EDX detector and operated at 200 kV. The Si NWs were harvested from the growth substrate by gently scraping into an ethanolic solution. The dispersion was then drop cast onto a grid of lacey carbon film (200 Mesh Nickel) for TEM imaging and analysis. X-ray diffraction patterns were collected on X'Pert (MSG-006) PRO MRD instrument fitted with X'celerator detector and a Cu Kα radiation source (λ = 1.5418 Å). The as synthesised M-seeded-Si NW anodes were electrochemically evaluated using two-electrode Swagelok cells. The half-cells were tested by pairing the as-prepared M-seeded-Si NW@3D Cu_xSi_y NF as working electrode with Li foil as the counter/reference electrode. A Celgard membrane was used as electrode separator and a solution of 1.0M $LiPF_6$ in ethylene carbonate/diethyl carbonate (1:1 v/v), mixed with 3% vinylene carbonate, as the electrolyte. All cells were assembled in an Ar-filled glovebox and then galvanostatically cycled within the potential range of 1.0–0.011 V (vs. Li/Li^+) at room temperature using a Biologic MPG-2 electrochemical workstation.

Supporting Information

Supporting Information is available from the Wiley Online Library or from the authors.

Acknowledgements

This work was supported by the Science Foundation Ireland (SFI) under the Principal Investigator Program under contract nos. 16/IA/4629 and 11-PI-1148 and under grant no. SFI 16/M-ERA/3419. This project has also received funding from the European Union's Horizon 2020 Research and Innovation Program under grant agreement no. 814464 (Si-DRIVE project).

H.G. acknowledges the SIRG under grant no. 18/SIRG/5484 and Enterprise Ireland under contract no. CF20144014. KMR further acknowledges IRCLA/2017/285 and SFI Research Centres MaREI, AMBER and CONFIRM 12/RC/2278_P2, 12/RC/2302_P2, and 16/RC/3918. We thank Bernal Institute Instrument Scientist (Dr. Vasily Lebedev) for help with HR-TEM imaging.

Conflict of Interest

The authors declare no conflict of interest

[1] T. D. Bogart, D.Oka, X. Lu, M. Gu, C. Wang, B. A. Korgel, *ACS Nano* **2014**, *8*, 915.

[2] G. Zhou, L. Xu, G. Hu, L. Mai, Y. Cui, *Chem. Rev*. **2019**, *119*, 11042.

[3] a) N. Liu, L. Hu, M. T. McDowell, A. Jackson, Y. Cui, *ACS Nano* **2011**, *5*, 6487; b) Y. Jin, B. Zhu, Z. Lu, N.Liu, J. Zhu, *Adv. Energy Mater*. **2017**, *7*, 1700715.

[4] C. K. Chan, H. Peng, G. Liu, K. McILwrath, X. F. Zhang, R. A. Huggins, Y. Cui, *Nat. Nanotechnol*. **2008**, *3*, 31.

[5] J. Yang, M. Winter, J. O. Besenhard, S*olid State Ionics* **1996**, *90*, 281.

[6] Y. Liu, M. Sun, Y. Yuan, Q. Wu, H. Wang, Y. He, Z. Lin, F. Zhou, M. Ling, C. Qian, C. Liang, J. Lu, *Adv. Funct. Mater*. **2020**, *30*, 1910249.

[7] A. M. Chockla, T. D. Bogart, C. M. Hessel, K. C. Klavetter, C. B. Mullins, B. A. Korgel, *J. Phy. Chem. C* **2012**, *116*, 18079.

[8] L. Mai, X. Tian, X. Xu, L. Chang, L. Xu, *Chem. Rev.* **2014**, *114*, 11828.

[9] T. Kennedy, M Brandon, F. Laffir, K. M. Ryan, *J. Power Sources* **2017**, *359*, 601.

[10] R. S. Wagner, W. C. Ellis, *Appl. Phys. Lett.* **1964**, *4*, 89.

[11] H. Geaney, C. Dickinson, C. O'Dwyer, E. Mullane, A. Singh, K. M. Ryan, *Chem. Mater.* **2012**, *24*, 4319.

[12] E. Dodony, G. Z. Radnóczi, I. Dódony, *Intermetallics* **2019**, *107*, 108.

[13] H. Song, S. Wang, X. Song, H. Yang, G. Du, L. Yu, J. Xu, P. He, H. Zhou, K. Chena, *J. Mater. Chem. A* **2018**, *6*, 7877.

[14] K. Stokes, H. Geaney, M. Sheehan, D. Borsa, K. M. Ryan, *Nano Lett*. **2019**, *19*, 8829.

[15] W. Zhou, C. Cheng, J. Liu, Y. Y. Tay, J. Jiang, X. Jia, J. Zhang, H. Gong, H. H. Hng, Ting Yu, H. J. Fan, *Adv. Funct. Mater*. **2011**, *21*, 2439.

[16] Q. Zhang, H. Chen, L. Luo, B. Zhao, H. Luo, X. Han, J. Wang, C. Wang, Y. Yang, T. Zhu, M. Liu, *Energy Environ. Sci.* **2018**, *11*, 669.

[17] S. Jing, H. Jiang, Y. Hu, C. Li, *Nanoscale* **2014**, *6*, 14441.

[18] F. A. Güneş, *RSC Advances* **2016**, *6*, 1678.

[19] H. Geaney, G. Bree, K. Stokes, G. A. Collins, I. S. Aminu, T. Kennedy, K, M. Ryan, *Chem. Commun*. **2019**, *55*, 7780.

[20] Q. Xiao, Y. Fan, X. Wang, R. A. Susantyokoa, Q. A. Zhang, *Energy Environ. Sci*. **2014**, *7*, 655.

[21] C. J. Zhang, S.-H. Park, A. S. Ascaso, S. Barwich, N. McEvoy, C. S. Boland, J. N. Coleman, Y. Gogotsi, V. Nicolos, *Nat. Commun*. **2019**, *10*, 849.

[22] a) B. Wang, J. Ryu, S. Choi, X. Zhang, D. Pribat, X. Li, L. Zhi, S. Park, R. S. Ruoff, *ACS Nano* **2019**, *13*, 2307; b) N. Liu, Z. Lu, J. Zhao, M. T. McDowell, H.-W. Lee, W. Zhao, Y. Cui, *Nat. Nanotechnol*. **2014**, *9*, 187.

[23] Z. Chen, J.W. F. To, C. Wang, Z. Lu, N. Liu, A. Chortos, L. Pan, F. Wei, Y. Cui, Z. Bao, *Adv. Energy Mater*. **2014**, *4*, 1400207.

[24] M. Zhou, X. Li, B. Wang, Y. Zhang, J. Ning, Z. Xiao, X. Zhang, Y. Chang, L. Zhi, *Nano Lett*. **2015**, *15*, 6222.

[25] F. Dogan, L. D. Sanjeewa S. J. Hwu, J. T.Vaughey, *Solid State Ionics* **2016**, *288*, 204.

[26] L. Hu, H. Wu, S. S. Hong, L. Cui, J .R. McDonough, S. Bohy, Y.Cui, *Chem. Commun*. **2011**, *47*, 367.

[27] J. K.Shon, H. S. Lee1, G. O. Park, J. Yoon, E. Park, G. S. Park, S. S. Kong, M. Jin, J.-M. Choi, H. Chang, S. Doo, J. M. Kim, W.-S. Yoon, C. Pak, H. Kim, G. D. Stucky *Nat. Commun*. **2015**, *6*, 7393.

[28] Z. Sun, D. N. Seidman, L. J. Lauhon, *Nano Lett*. **2017**, *17*, 4518.

[29] M. Sheehan, Q. M. Ramasse, H. Geaney, K. M. Ryan, *Nanoscale* **2018**, *1*, 19182.

[30] X. Li, J.-H. Cho, N. Li, Y. Zhang, D. Williams, S. A. Dayeh, S. T. Picraux, *Adv. Energy Mater*. **2012**, *2*, 87.

[31] K. Stokes, H. Geaney, G. Flynn, M. Sheehan, T. Kennedy, K.M. Ryan, Anodes. *ACS Nano* **2017**, *11*, 10088.

[32] S.-H. Park, P. J. King, R. Tian, C. S. Boland, J. Coelho, C. J. Zhang, P. McBean, N. McEvoy, M. P. Kremer, D. Daly, J. N. Coleman, V. Nicolosi, *Nature Energy* **2019**, *4*, 560.

[33] E. R. Hemesath, D. K. Schreiber, E. B. Gulsoy, C. F. Kisielowski, A. K. Petford-Long, P. W. Voorhees, L. J. Lauhon, *Nano Lett*. **2012**, *12*, 167.

[34] a) H. Chen, M. Li, Z. Lu, X. Wang, J. Yang, Z. Wang, F. Zhang, C. Gu, W. Zhang, Y. Sun, J. Sun, W. Zhu, X. Guo, *Nat. Commun*. **2019**, *10*, 3872; b) W. F. Lange, M. Enomoto, H. I. Aaronson, *Int. Mater. Rev*. **1989**, *34*, 125.

[35] N. Nitta, F. Wu, J. T. Lee, G. Yushin, *Mater. Today* **2015**, *18*, 252.

[36] G.T. Kim, T. Kennedy, M. Brandon, H. Geaney, K. M. Ryan, S. Passerini, G.B. Appetecchi, *ACS Nano* **2017**, *11*, 5933.

[37] A. I. Hochbaum, P. Yang, *Chem. Rev*. **2010**, *110*, 527.

[38] M. Gu, Z. Wang, J. G. Connell, D. E. Perea, L. J. Lauhon, F. Gao, C. Wang, *ACS Nano* **2013**, *7*, 6303.

[39] H. Wu, G. Chan, J. W. Choi, I. Ryu, Y. Yao, M.T. McDowell, S.W. Lee, A. Jackson, Y. Yang, L. Hu, Y. Cui, *Nat. Nanotechnol*. **2012**, *7*, 310.

[40] T. Kennedy, E. Mullane, H. Geaney, M. Osiak, C. O'Dwyer, K.M. Ryan, *Nano Lett*. **2014**, *14*, 716.

[41] C. S. Wang, G.T. Wu, X. B. Zhang, Z. F. Qi, W. Z. Li, *J. Electrochem. Soc*. **1998**, *145*, 2751.

[42] H. Li, X. Huang, L. Chen, Z. Wu, Y. Liang, *Electrochem. Solid St. Lett.* **1999**, *2*, 547.

[43] K. Stokes, G. Flynn, H. Geaney, G. Bree, K. M. Ryan, *Nano Lett*. **2018**, *18*, 5569.

The table of contents entry

A novel 3D network of binary-phase Cu-silicide nanofoam (3D Cu_xSi_y NF) is designed as a current collector that facilitates high-density/single-phase Si NW growth with an areal-loading in excess of 1.0 mg cm^{-2} and an areal-capacity of ~2.0 mAh cm^{-2} after 550 cycles. The nanofoam also enables Al, Bi, Cu, In, Mn, Ni, Sb, Sn and Zn mediated Si NW growth, demonstrating the universality of the anode architecture.

Keywords: 3D Cu_xSi_y nanofoam, silicon nanowires, high density, areal capacity, lithium-ion battery

Ibrahim Saana Aminu, Hugh Geaney, Sumair Imtiaz, Temilade E. Adegoke, Nilotpal Kapuria, Gearoid A. Collins, Kevin M. Ryan*

Title: A Copper Silicide Nanofoam Current Collector for Directly Grown Si Nanowire Networks and their Application as Lithium-ion Anodes

ToC Figure